International Journal of Rock Mechanics & Mining Sciences 183 (2024) 105939



Contents lists available at ScienceDirect

International Journal of Rock Mechanics and Mining Sciences

journal homepage: www.elsevier.com/locate/ijrmms





Geothermal fluid extraction and injection-related fracture slip susceptibility and seismicity in naturally fractured rocks

Wenzhuo Cao [a,*,1], Sevket Durucan [a], Ji-Quan Shi [a], Anna Korre [a], Thomas Ratouis [b], Vala Hjörleifsdóttir [c,2]

[a] Department of Earth Science and Engineering, Royal School of Mines, Imperial College London, London, United Kingdom
[b] Carbfix, Smáratorg 3, 201, Kópavogur, Iceland
[c] Orkuveita Reykjavíkur (Reykjavík Energy), Bæjarhálsi 1, 110, Reykjavik, Iceland

ARTICLE INFO

Keywords:
Geothermal exploitation
Fracture system
Induced seismicity
Thermo-hydro-mechanical coupling
Cooling contraction
Fluid overpressure

ABSTRACT

Understanding fracture slip susceptibility in geothermal reservoirs is central to the control of fluid injection-induced seismicity. To investigate the role of regional fracture systems on induced seismicity, a coupled thermo-hydro-mechanical (THM) model containing fracture networks was developed, which features direct coupling between different physics for explicit fractures, fractured rocks (porous matrix blocks with small-scale fractures) and their interactions, as well as indirect coupling through changes of material properties, such as stress-dependent fracture and rock permeabilities. The model was applied to simulate geothermal fluid extraction and re-injection in a natural fracture system comprised of three dominant fracture sets at the Hellisheiði geothermal field over a 10-year period (2011–2021), utilising field recorded monthly production and re-injection rates. Based on the model results, the slip susceptibility of regional fracture systems was examined under reservoir conditions before and after the start of fluid re-injection across different time scales, i.e., over short (1 month), intermediate (1 year) and long-term (10 years). Two model scenarios, one with cooling contraction and one without, were considered to examine the relative contribution of cooling contraction and fluid overpressure on fracture slip susceptibility. Results have shown that fracture networks act as preferential fluid flow paths that influence fluid pressure and stress distribution and fracture slip susceptibility in geothermal reservoirs. NE-SW and N-S trending fractures at Hellisheiði are susceptible to slippage before the start of fluid re-injection. During fluid re-injection, the distribution of fractures with enhanced slip susceptibility gradually shifts from surrounding the re-injection region to forming a two-lobed pattern in the fault-normal direction around the re-injection region, indicating the dominant role of cooling contraction over fluid overpressure on the fracture slip susceptibility in the intermediate- and long-term.

1. Introduction

Induced seismicity associated with subsurface fluids injection have been a longstanding concern in industrial geothermal applications. In addition to fluid injection operations, regional fracture systems that form preferential fluid flow pathways exert fundamental controls on the induced seismic occurrence.[1–3] The high correlation between induced seismicity and characteristic of regional fracture systems has also been observed in various industrial applications, including oil and natural gas extraction (e.g., Groningen gas field, and Permian Basin of West Texas and Southeast New Mexico),[4,5] wastewater injection (e.g., Oklahoma, and Fort Worth Basin of Texas),[3,6–8] and geothermal exploitation (e.g., Matouying geothermal field).[9] Most induced seismicity occurred on fault structures or fracture traces that have relatively high slip tendency in the existing stress field. Induced seismicity sequences tend to orient aligned with fault structures along with the maximum horizontal principle stress.[5,6,10] In fault systems that accommodate multiple injection wells, the majority of mapped faults may have a likelihood to slip that is equal to or greater than that of faults that have already hosted induced seismic events.[6]

* Corresponding author.
E-mail address: w.cao2@uu.nl (W. Cao).
[1] Present addresses: Department of Earth Sciences, Utrecht University, the Netherlands.
[2] Present addresses: Department of Engineering, Reykjavik University, Iceland.

https://doi.org/10.1016/j.ijrmms.2024.105939
Received 20 May 2024; Received in revised form 8 October 2024; Accepted 12 October 2024
Available online 28 October 2024
1365-1609/© 2024 The Authors. Published by Elsevier Ltd. This is an open access article under the CC BY-NC license (http://creativecommons.org/licenses/by-nc/4.0/).

A vital component in controlling induced seismicity is to identify potentially active fractures or faults amongst regional fracture systems or fault traces, and to evaluate conditions that likely promote slip. To this end, substantial efforts have been made on the evaluation of fault/fracture behaviour under fluid injection conditions through deterministic geomechanical modelling. Geochemical models were usually coupled with hydrological models to obtain spatial and temporal distribution of fluid pressure and stress field surrounding injection wells. The focus has been placed on modelling the fault/fracture behaviour not only in terms of slippage and stress re-distribution, but also fluid flow and even convective heat transfer. In earlier studies, fractures implemented in numerical models have mostly been simplistic major fractures[11–13] or statistically generated discrete fractures.[14–17] Recently, researchers have considered field realistic fault traces or fracture systems, comprised of a set of planar fault/fracture segments.[18–20] A wide variety of indicators were used to examine the stability of faults/-fractures, such as the fault slippage magnitude,[20] horizontal fault slip rate,[18] and Coulomb failure stress change.[21,22]

In addition to geomechanical modelling, the slip-tendency analysis for fractures provides a rapid evaluation of stress in terms of its potential to cause slip, or seismic susceptibility in regions prone to seismicity.[23,24] This analysis is based on the notion that fault or fracture slip is determined by the ratio of resolved shear to normal stress on the fault or fracture plane in the ambient stress field, following the linearised Mohr-Coulomb fracture slip criterion. In recent years, a probabilistic approach to assess the fault slip potential based on the slip-tendency analysis has been developed and applied to various field sites.[5,6,9,10] This probabilistic approach incorporates uncertainties in Mohr-Coulomb parameters, including fault strike and slip, rock properties, initial fluid pressure and ambient stress field. This approach uses the Monto Carlo method to generate numerous random combinations of parameters, and calculates the probability of slip at specified fluid pressure on fault or fracture segments, referred to as the fault-slip potential (FSP). However, these deterministic and probabilistic seismic susceptibility evaluation methods for realistic fracture systems or fault structures were mostly based on fluid overpressure alone (e.g. Refs. 10, 25,26), neglecting the poroelastic and thermoelastic stressing effects that also significantly contribute to induced seismicity. In particular, thermal effects caused by cold fluids injection in geothermal exploitation may play a dominant role in induced seismicity occurrence,[27] but was seldom considered. Therefore, it is essential to employ coupled thermo-hydro-mechanical (THM) numerical models to resolve interactions and complexities involved in various subsurface processes and accurately reflect their impacts on the slip tendency.[28]

The authors[27] have carried out fully coupled THM modelling of fluid re-injection into the Húsmúli area through five re-injection wells under constant injection pressure conditions to evaluate the potential for induced seismicity over a 1-year period (2011–2012) at the Hellisheiði geothermal field. Not explicitly representing regional fracture systems, this model was not able to reflect finer-scale, preferential fluid flow pathways,[29,30] nor to correlate seismic susceptibility with slip tendency of fractures. In addition, multiple years of fluid extraction and re-injection with time-varying production and injection rates could complicate the fluid flow and heat transfer behaviour in the reservoir, which significantly influence the fracture slip behaviour and seismic response.

The objective of this follow-up work was two-fold: 1) to investigate the role of regional fracture systems on geothermal fluid production and re-injection induced seismicity, and 2) to examine the competing role of fluid pressure and cooling contraction on the reservoir response and fracture slip susceptibility across different time scales. Field mapped fracture network level preferential fluid flow paths at the Hellisheiði geothermal field were implemented into a fully coupled THM model, which features direct coupling between different physics for explicit fractures, fractured rocks (porous matrix blocks with small-scale fractures) and their interactions, as well as indirect coupling through changes of material properties, such as stress-dependent fracture and rock permeabilities. The model was applied to simulate the geothermal fluid extraction at the Skarðsmýrarfjall area (through six production wells) and re-injection at the Húsmúli area (through five re-injection wells) over a 10-year period (2011–2021), utilising field recorded monthly production and re-injection rates. Based on the model results, the slip susceptibility of regional fracture systems was examined under in-situ conditions as well as after geothermal operations. Two modelling scenarios, one considering the poroelastic effect and the other thermo-poroelastic effect, were examined to identify the areal extent and evolution of cooling contraction and fluid overpressure, and their relative contributions to slip susceptibility for fractures across short (1 month), intermediate (1 year) and long-term (10 years) time frames.

2. Hellisheiði geothermal field

Located in the Southwest Iceland, the Hellisheiði geothermal field produces geothermal fluid at 240–320 °C from a reservoir at depths ranging from 1.5 to 3.3 km. The subsurface at the geothermal field is comprised of a succession of hyalocalstic and olivine tholeiitic basaltic sequences.[30] The region consists of NNE-SSW trending extensional fault structures with sub-vertical dips and highly fractured fissure swarms. The maximum horizontal principal stress is oriented in alignment with regional major fault structures. The vertical principal stress gradient σ_v is 29.5 MPa/km, and maximum and minimum horizontal principal stress gradients are constrained in the range of 71.3–76.0 and 13.0–29.5 MPa/km, respectively.[31]

Fluid flow at the Hellisheiði geothermal field is controlled by regional fault structures, which provide favourable fluid conduits along the fault strike but impede fluid flow across faults. Regional fracture systems have been identified from outcrop fractures mapped using aerial imagery, and processed using three types of imageries, including coloured Spot, coloured Orthomaps, and black and white aerial photographs.[32] Fracture traces were first observed on Spot images having a resolution of ~5 m on the ground surface. Then, these traces were examined with Orthomaps (having a resolution of ~1 m on the ground surface) and aerial photographs for corrections in fine detail and the determination of relative ages. Fractures identified were categorised into three sets based on orientations (Fig. 1a)[30,32,33].

- Set 1: NE-SW trending (NNE, NE and ENE). Parallel or sub-parallel to regional fault strikes, this Set extends from the Húsmúli re-injection area to the edge of the Skarðsmýrarfjall production area, facilitating the subsurface fluid circulation.
- Set 2: N-S trending (N and NNW). This Set channels fluid flow from and to NE-SW trending fractures.
- Set 3: NW-SE trending (WNW and EW). Perpendicular to regional fault strikes, this Set delays fluid travel time across fractures.

The fracture frequency was quantified in terms of the number of fracture segments and the total length of fractures by orientation (Fig. 1b and c). Based on the total fracture length by orientation, the three fracture sets are almost equally frequent, followed by fractures in other orientations. Sets 1 and 2 are carrier structures providing preferable fluid flow paths, and Set 3 represents barrier structures that impede the fluid flow. The fractures have near-vertical structures as evidenced from well log observations.[33]

One main production zone at the Hellisheiði geothermal field, the Skarðsmýrarfjall area, has six production wells (HE05, HE31, HE33, HE44, HE46 and HE48), and annually produces ~10 Mt of geothermal fluids. The main re-injection site, the Húsmúli area, has five injection wells (HN09, HN12, HN14, HN16 and HN17) and re-injects ~12 Mt of spent geothermal fluid annually. Fluid injection activities started on September 1, 2011 at wells HN09, HN12, HN14 and HN17, and on 23 September at well HN16.[34] Over the 10-year period from September 2011 to December 2021, injection rates at the five injection wells

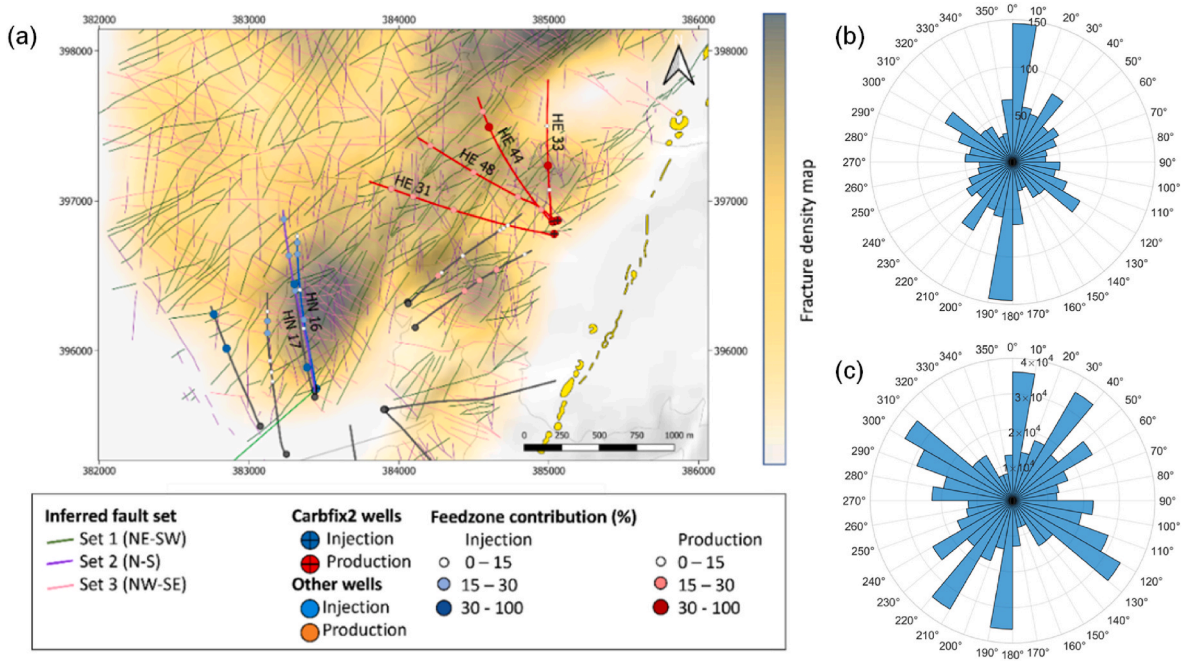


Fig. 1. Fracture systems in the Northwest section of the Hellisheiði geothermal field (Húsmúli and Skarðsmýrarfjall areas): (a) fracture trace and density map (after[30]), and statistics of fractures, including (b) rose diagram for the number of fracture segments, and (c) rose diagram for the total fracture length (after[32]).

fluctuated mostly between 50 and 100 kg/s, with wellhead pressures being maintained at ~8 bar (Fig. 2). The temperature of re-injected fluids varied between 70 and 100 °C.

3. Coupled THM modelling methodology

The coupled THM model used for simulating the fluid extraction and re-injection related reservoir behaviour considers direct coupling between different physics (fluid flow, heat transfer and geomechanics) for explicit fractures, fractured rocks and their interactions (Sections 3.1-3.3), as well as indirect coupling through changes in material properties, such as stress-dependent rock and fracture permeabilities (Section 3.4). Fractured rocks are considered as interacting continua comprised of porous matrix blocks and fully penetrating small-scale fractures that are not explicitly represented, whilst large-scale fractures are explicitly considered as lower-dimension thin layers (individual fractures) that are subjected to ambient stresses and fluid pressure. Fig. 3 illustrates the modelling methodology for geothermal fluid extraction and re-injection in a naturally fractured thermoporoelastic porous media, comprised of a deformable fractured rock domain and explicitly embedded large-scale discrete fractures.

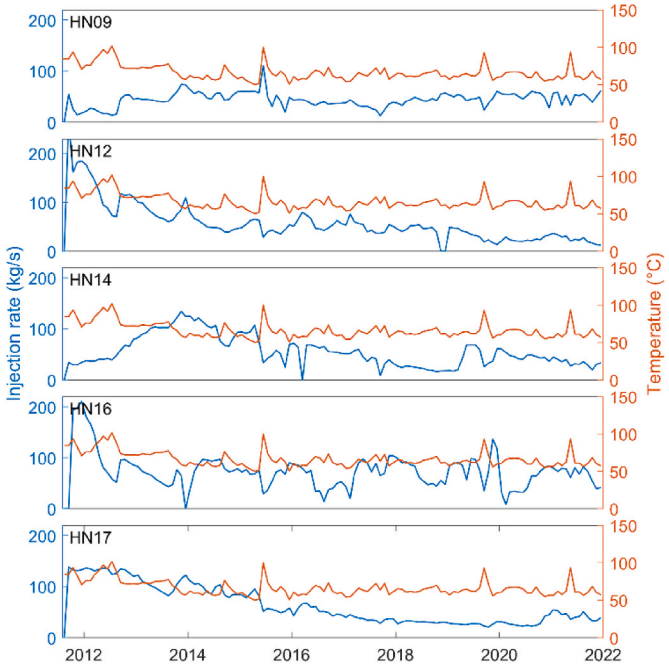


Fig. 2. Fluid injection rate and temperature time series at five re-injection wells (HN09, HN12, HN14, HN16 and HN17) at the Húsmúli area during September 2011–December 2021.

3.1. Fluid flow

Mass conservation equations with the Darcy's law govern fluid flow through both fractured rocks and explicit fractures[1]:

$$\rho S_{\mathrm{m}} \frac{\partial p}{\partial t} + \nabla \cdot (\rho \boldsymbol{v}_{\mathrm{m}}) = Q_{\mathrm{f}} - \rho \alpha \frac{\partial \varepsilon_{\mathrm{V}}}{\partial t}, \tag{1}$$

$$\boldsymbol{v}_{\mathrm{m}} = -\frac{k_{\mathrm{m}}}{\mu} \nabla p, \tag{2}$$

and

$$b \rho S_{\mathrm{f}} \frac{\partial p}{\partial t} + \nabla_{\tau} \cdot (b \rho \boldsymbol{v}_{\mathrm{f}}) = \rho \left(f_{\mathrm{up}} + f_{\mathrm{bottom}} \right) - \rho \frac{\partial b}{\partial t}, \tag{3}$$

$$\boldsymbol{v}_{\mathrm{f}} = -\frac{k_{\mathrm{f}}}{\mu} \nabla_{\tau} p, \tag{4}$$

where ρ is the fluid density, Q_{f} is the mass source term, α is the Biot coefficient, ε_{V} is the volumetric strain, and μ is the dynamic viscosity of fluids. $\boldsymbol{v}$, k and S are the Darcy's velocity vector, permeability and poroelastic storage coefficient, with subscripts "m" and "f" representing fractured rocks or explicit fractures, respectively. $f_{\mathrm{i}} = -(k_{\mathrm{m}}/\mu)(\partial p_{\mathrm{i}}/\partial n_{\mathrm{i}})$ is the fluid exchange term between fractured rocks and explicit fractures, with subscript i denoting the up or bottom side of the explicit fracture and n_{i} representing the outward normal direction of the fracture wall. ∇_{τ}

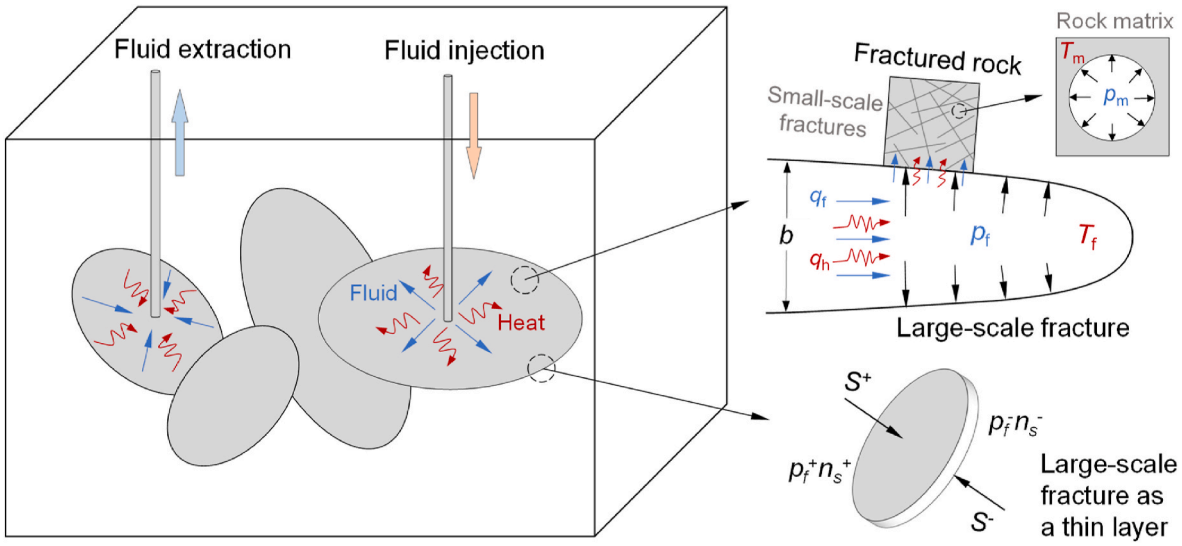


Fig. 3. Schematic diagram for simulating fluid extraction and re-injection using the coupled THM model, considering a deformable fractured rock domain (porous matrix blocks and implicitly embedded small-scale fractures) and explicitly embedded large-scale discrete fractures (modified from[11,35]).

is the gradient operator restricted to the fracture's tangential plane. The solid-to-fluid coupling is reflected by the influence of pore volume and fracture aperture on the fluid pressure.

3.2. Heat transfer

Heat transfer follows thermal energy balance equations in both fractured rocks and explicit fractures, where variations of thermal energy in time are balanced by convection driven by the Darcy's velocity field, and thermal conduction governed by the Fourier's law. The thermal energy balance equations are written as[1]:

$$(\rho C)_{\mathrm{eff}}\frac{\partial T}{\partial t}+\rho_{\mathrm{f}}C_{\mathrm{f}}\boldsymbol{v}_{\mathrm{m}}\cdot\nabla T+\nabla\cdot(\boldsymbol{q}_{\mathrm{m}})=Q_{\mathrm{h}}, \tag{5}$$

$$\boldsymbol{q}_{\mathrm{m}}=-k_{\mathrm{eff}}\nabla T, \tag{6}$$

and

$$b(\rho C)_{\mathrm{eff}}\frac{\partial T}{\partial t}+b\rho_{\mathrm{f}}C_{\mathrm{f}}\boldsymbol{v}_{\mathrm{f}}\cdot\nabla_{\tau}T+\nabla_{\tau}\cdot\boldsymbol{q}_{\mathrm{f}}=e_{\mathrm{up}}+e_{\mathrm{bottom}}, \tag{7}$$

$$\boldsymbol{q}_{\mathrm{f}}=-bk_{\mathrm{eff}}\nabla_{\tau}T, \tag{8}$$

where T is temperature, Q_{h} is the heat source term, and $\boldsymbol{q}$ is the conductive heat flux, with subscripts "f" and "r" denoting fluids and fractured rocks, respectively. Terms $(\rho C)_{\mathrm{eff}}=\phi\rho_{\mathrm{f}}C_{\mathrm{f}}+(1-\phi)\rho_{\mathrm{r}}C_{\mathrm{r}}$ and $k_{\mathrm{eff}}=\phi k_{\mathrm{f}}+(1-\phi)k_{\mathrm{r}}$ are the effective heat capacity and effective thermal conductivity, respectively, where ϕ is the fractured rock porosity, and ρ, C and k are the density, specific heat capacity and thermal conductivity for fluids and fractured rocks, respectively. $e_{\mathrm{i}}=\rho_{\mathrm{f}}C_{\mathrm{f}}T_{\mathrm{i}}f_{\mathrm{i}}-k_{\mathrm{eff}}\cdot\partial T_{\mathrm{i}}/\partial n_{\mathrm{i}}$ is the convective and conductive heat exchange term between fractured rocks and explicit fractures, with subscript i denoting the up or bottom side of the fracture. The heat exchange in geothermal environments is usually dominated by the convection,[36] which reflects the hydrological effect on the temperature field.

3.3. Geomechanical deformation

Stress equilibrium of fractured porous media satisfies the momentum balance equation, which is expressed by:

$$\nabla\cdot\boldsymbol{\sigma}+\boldsymbol{F}=0, \tag{9}$$

where $\boldsymbol{\sigma}$ denotes the total stress tensor, and $\boldsymbol{F}$ is the body force vector. Geomechanical deformation of fractured rocks is calculated based on the total strain, which is comprised of the stress-free strain caused by fluid pressure and temperature changes, and thermoporoelastic strain induced by the thermoporoelastic stress[21]:

$$\boldsymbol{\varepsilon}=\frac{1}{2G}\left(\boldsymbol{\sigma}-\frac{\nu}{1+\nu}tr\boldsymbol{\sigma}\right)+\frac{\alpha}{3K}p\boldsymbol{I}+\alpha_T\Delta T\boldsymbol{I}, \tag{10}$$

where G, K and ν are the shear modulus, bulk modulus and Poisson's ratio of fractured rocks, respectively. α and α_{T} are the Biot coefficient and thermal expansion coefficient, respectively. $\boldsymbol{\varepsilon}$ is the total strain tensor, which is expressed by the displacement vector $\boldsymbol{u}$, i.e., $\boldsymbol{\varepsilon}=(\boldsymbol{u}\nabla+\nabla\boldsymbol{u})/2$, and $\boldsymbol{I}$ is the unit tensor. ΔT is the temperature change. This constitutive relationship represents hydrological and thermal effects on the displacement field.

The effective stress tensor $\boldsymbol{\sigma}'$ is related to the total stress tensor $\boldsymbol{\sigma}$:

$$\boldsymbol{\sigma}'=\boldsymbol{\sigma}+\alpha p\boldsymbol{I}. \tag{11}$$

Fractures subjected to stress perturbations may manifest normal opening and closure, and shear deformation behaviour. In compressive environments, the fracture normal closure u_{n} is described by a hyperbolic relationship with the prevailing effective normal stress σ_{n}', i.e., Barton-Bandis joint deformation model[37]:

$$u_{\mathrm{n}}=\frac{\sigma_{\mathrm{n}}'u_{\mathrm{m}}}{k_{\mathrm{n0}}u_{\mathrm{m}}+\sigma_{\mathrm{n}}'}, \tag{12}$$

where k_{n0} is the initial fracture normal stiffness, and u_{m} is the maximum allowable closure approximated by the fracture aperture under unstressed conditions. Under tensile stress, the fracture tensile opening u_{n} is given by:

$$u_{\mathrm{n}}=\sigma_{\mathrm{n}}'/k_{\mathrm{n0}}. \tag{13}$$

Similarly, the fracture shear deformation u_{s} is obtained by the fracture shear stiffness k_{s} and the prevailing shear stress τ_{s}:

$$u_{\mathrm{s}}=\tau_{\mathrm{s}}/k_{\mathrm{s}}. \tag{14}$$

3.4. Stress-dependent permeability

Permeabilities for both fractured rocks and explicit fractures are stress dependent. The permeability of fractured rocks k_{m} varies with rock porosity ϕ as follows[38,39]:

$$\frac{k_m}{k_0} = \left(\frac{\phi}{\phi_0}\right)^3, \tag{15}$$

where k_0 and ϕ_0 are the rock permeability and porosity at unconfined stress, respectively. The rock porosity ϕ is given by[40–42]:

$$\phi = (\phi_0 - \phi_r)\exp\left(\alpha_\phi \overline{\sigma}_v\right) + \phi_r, \tag{16}$$

where ϕ_r is the residual porosity at high stress, $\overline{\sigma}_v$ is the mean effective stress (with tension positive, in Pa), and α_ϕ is the stress sensitivity coefficient (with a value of 5.0×10^{-8}/Pa for typical rocks).[40,42,43]

The fracture permeability k_f is related to the fracture aperture b based on the cubic law:

$$k_f = \frac{b^2}{12}, \tag{17}$$

where the fracture aperture b varies depending on whether the fracture is under compressive or tensile stress:

$$b = \begin{cases} b + u_n, & \sigma_n' < 0 \\ b - u_n, & \sigma_n' \geq 0 \end{cases}. \tag{18}$$

The stress dependence of both fracture and rock permeabilities represents the mechanical effect on the hydrological field, and in turn the temperature field.

4. Numerical modelling of geothermal operations in fractured rocks

A 2D THM coupled model incorporating extracted fracture networks was constructed to simulate the geothermal fluid extraction and re-injection related reservoir behaviour and to evaluate the slip susceptibility of fractures systems over a 10-year period at 1000 m depth at the Hellisheiði geothermal field (Húsmúli and Skarðsmýrarfjall areas). The stratigraphy at the target depth mainly consists of the hyalocalistic formation, which are underlain by basaltic basement (from ~1600 m down to 3300 m depth). The fracture system explicitly considered in the

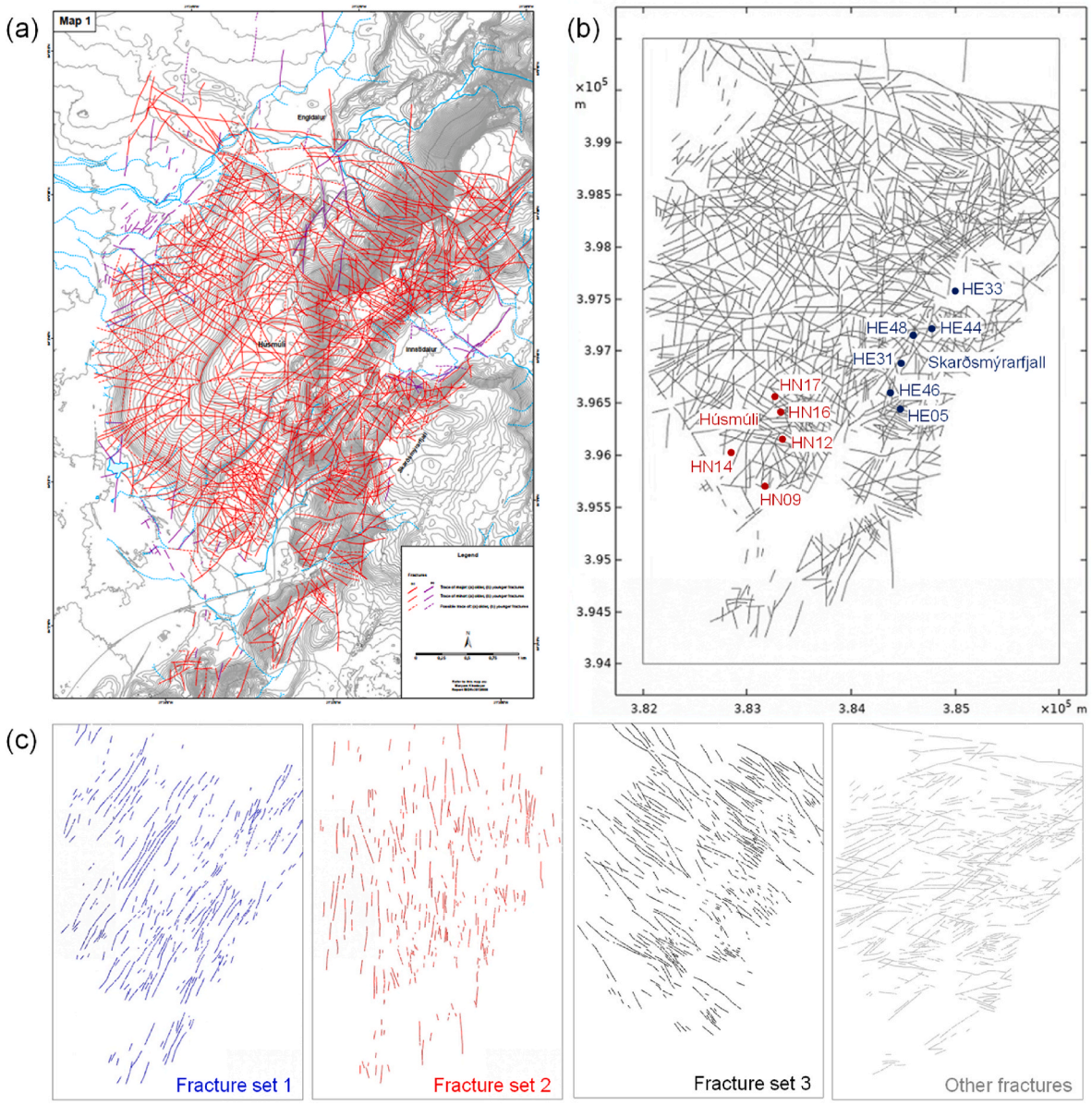


Fig. 4. Model geometry for the 2D coupled THM model incorporating fracture networks at the Hellisheiði geothermal field (Húsmúli and Skarðsmýrarfjall areas): (a) the full fracture network mapped (after[30,32]), (b) model geometry and locations of five re-injection wells at Húsmúli and six production wells at Skarðsmýrarfjall, and (c) three dominant fracture sets and other fractures at Húsmúli and Skarðsmýrarfjall.

model (Fig. 4b), including the three dominant fracture sets (Fig. 4c), was extracted and digitalised from the full set of outcrop fractures mapped (Fig. 4a).[32] Each fracture was discretised as a set of fracture segments having a minimum length of 5 m.

The equivalent permeability of fractured rocks can be derived under steady state uniform flow conditions based on the Darcy's law. Given a rock matrix permeability of 0.1 mD (=0.1 × 10^{-15} m^2), a fracture permeability in the range of 15–50 mD, and a fracture volume fraction of 5 % for the hyalocalistic formation,[30] the effective permeability of fractured rocks ranges between 0.845 and 2.595 mD. Therefore, an initial fractured rock permeability of 2 mD was used in the model. This single-porosity model for reservoir rocks may not reflect the local thermal non-equilibrium due to the relatively slow heat transfer between explicit fractures and fractured rocks, but is considered to capture well field-scale fluid flow and heat transfer in extensively fractured rocks at Hellisheiði.[44] Other geomechanical, hydrological and thermodynamic parameters for rocks were taken from[27] (Table 1).

Effective fracture permeabilities k_{eff} for different fractures sets were modelled based on fracture aperture b and fracture zone width h under prevailing in-situ stresses, given by $k_{eff} = b^3/(12h)$. One key fracture parameter is the initial fracture aperture b_0, which was uniformly assigned a value of 0.5 mm. Assuming a width of 10 m for fractured zones, the initial effective fracture permeability k_{eff} calculated under prevailing in-situ stresses for the three fracture sets are 10^3-10^4 mD (Set 1), ~10^3 mD (Set 2), and 10^1-10^2 mD (Set 3). These are in general agreement with permeability values used in Ratouis et al.[30]'s model, where corresponding values are 200-5000 mD (Set 1), 100-5000 mD (Set 2), and 50–150 mD (Set 3). This indicates that the coupled model could reproduce realistically anisotropic hydrological properties using the stress-dependent permeability relationship, based on a uniform initial fracture aperture. The verification of implementing implicitly embedded small-scale fractures and calibration of the coupled model against field measured injectivities can be referred to in.[27]

Table 1
Material properties of hyalocalistic formation used in the coupled THM model. Initial values for stress-dependent porosities and permeabilities at 1000 m depth in bold.

Parameters	Explicit fractures	Fractured rocks	References
Physical and mechanical properties			
Density ρ (kg/m^3)	–	2600	Ratouis et al.[30]
Young's modulus E (GPa)	–	60	Juncu et al.[34]
Poisson's ratio υ	–	0.25	Juncu et al.[34]
Initial normal stiffness k_{n0} (GPa/m)	50	–	
Initial shear stiffness k_{s0} (GPa/m)	10	–	
Hydrological properties			
Initial porosity ϕ	**0.1**	**0.1**	Stefánsson et al.,[45] Snæbjörnsdóttir et al.,[46] Ratouis et al.[30]
Residual porosity ϕ_r	–	0.01	
Initial permeability k (mD)	–	**2**	Ratouis et al.[30]
Initial fracture aperture b_0 (mm)	**0.5**	–	
Biot coefficient α	1	1	
Thermodynamic properties			
Heat capacity C_p (J/kg/K)	900	900	Ratouis et al.[30]
Thermal conductivity k_s (W/m/K)	1.5	1.5	Ratouis et al.[30]
Coefficient of thermal expansion α_T (1/K)	–	2 × 10^{-5}	Juncu et al.[47]

The model simulated the geothermal fluid extraction at Skarðsmýrarfjall and re-injection at Húsmúli during September 2011–December 2021. The stress field in the numerical model was first initialised by applying normal and shear components of in-situ stresses on model boundaries, considering a 200 m overburden. This ensures the maximum horizontal principal stress to be applied in the NNE-SSW direction. The in-situ fluid pressure field was calculated based on gravitational equilibrium, in additional to an overpressure of 20 bar caused by the local high natural groundwater table. Fluid extraction and re-injection were then modelled for the six production wells at Skarðsmýrarfjall and five re-injection wells at Húsmúli, using field fluid extraction and re-injection rate and temperature time series (see Fig. 2 for fluid re-injection rate and temperature time series).[30]

To investigate the respective role of fluid overpressure and cooling contraction on fracture slip susceptibility, two coupled model scenarios were considered: (1) non-cooling contraction model scenario (under poroelastic effect), and (2) cooling contraction model scenario (under thermoporoelastic effect). The stress-dependent permeability model was activated for the faulted reservoir domain in both model scenarios. A maximum timestep of 10 day was used in modelling for accuracy considerations.

To monitor fluid pressure, temperature and stress changes at different locations over the geothermal operation period, five measurement points spaced by 500 m were set up in the fault-parallel direction, and five spaced by 300 m in the fault-normal direction (see Fig. 5a and 8a). The measurement point A is located in between injection wells HN16 and HN17.

Based on modelled fluid pressure and stress distribution, the slip susceptibility of the fracture network was evaluated by means of the Coulomb failure stress change ΔCFS, using a friction coefficient of 0.6. Calculations were performed for each individual fracture segment based on its orientation.

5. Model results and analyses

5.1. Thermo-hydro-mechanical response of reservoir rocks

Fig. 5 presents the thermo-hydro-mechanical reservoir behaviour at 1000 m depth at the Hellisheiði geothermal field after 1 month, 1 year and 10 years of operations for both model scenarios. When the cooling contraction is not considered, fluid pressure is elevated around the Húsmúli area, and reduced around the Skarðsmýrarfjall area (Fig. 5a). The areal extent of both overpressurised and underpressurised regions experiences remarkable changes in response to fluctuating field injection and production rates (Fig. 2) throughout the entire injection period, indicating that fracture networks provides excellent hydraulic conductivities at the field site. In contrast, significant temperature decrease is observed around the five re-injection wells at the Húsmúli area, and this cooled region expands remarkably in the fault-parallel direction (the maximum principal stress direction) over the modelled period (Fig. 5b). In overpressurised regions around the Húsmúli area or underpressurised regions around the Skarðsmýrarfjall area, the bulk expansion or compression of rocks is resisted by poroelastic stress of a lesser amount than the fluid pressure change (mostly below 1 MPa). The combined effects of pore pressure and poroelastic stress lead to a decrease in the minimum effective principal stress change $\Delta\sigma'_3$ (less compressive, moving towards the Mohr-Coulomb fracture slip envelope) around the Húsmúli area, and an increase (more compressive, moving away from the Mohr-Coulomb fracture slip envelope) around the Skarðsmýrarfjall area (Fig. 5c).

When the cooling contraction is modelled, the overpressured region has similar areal extents at different times over the modelled period, as compared to in the non-cooling contraction model scenario (Fig. 5d). In contrast, cooled regions influenced by Darcy's velocity field expand not only in the fault-parallel direction, but also in the fault-normal direction

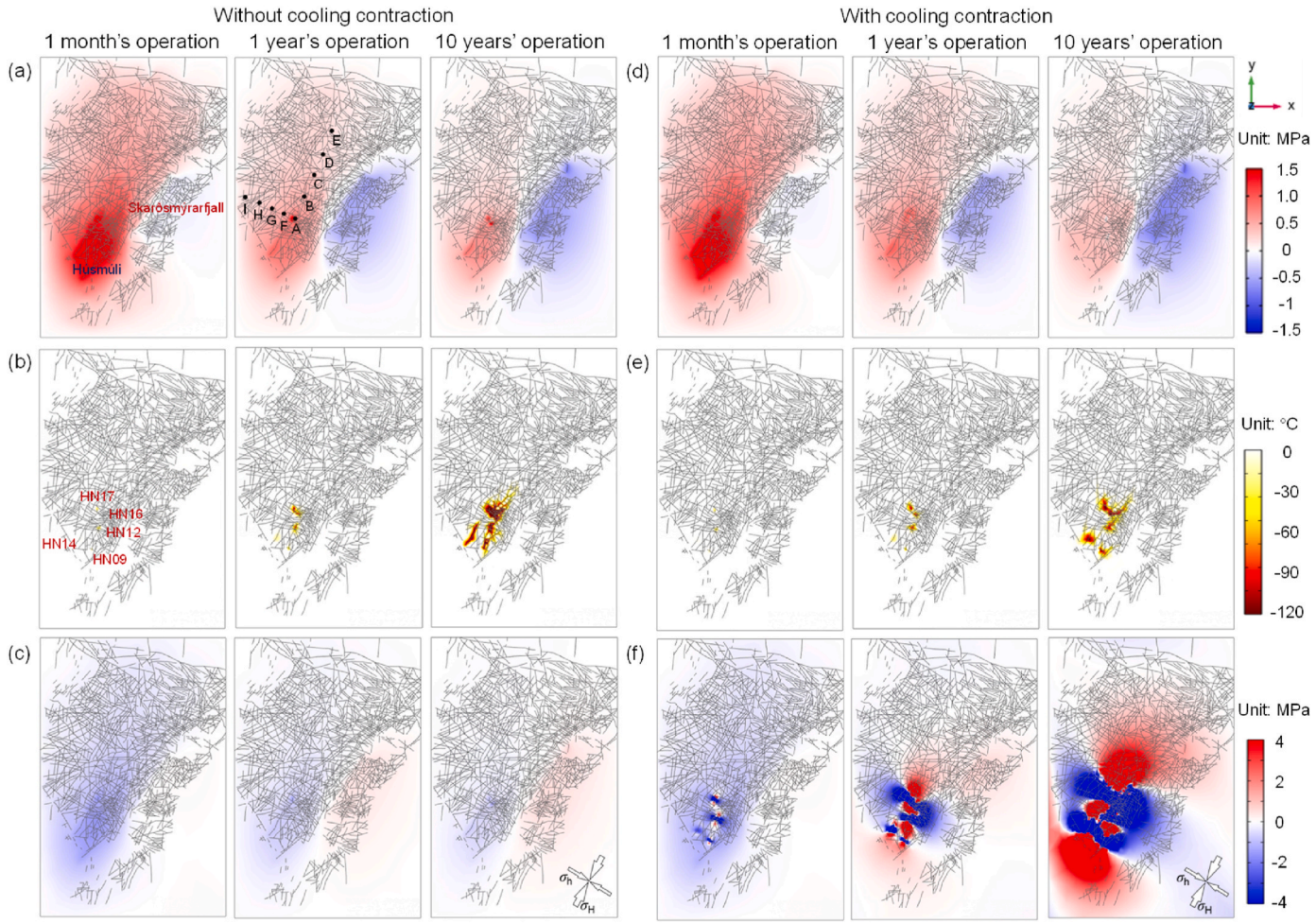


Fig. 5. Thermo-hydro-mechanical reservoir behaviour at 1000 m depth after 1 month, 1 year and 10 years of operations at the Hellisheiði geothermal field (Húsmúli and Skarðsmýrarfjall): (a) fluid pressure change Δp, (b) temperature change ΔT, and (c) minimum effective principal stress change $\Delta\sigma'_3$ (positive for compression).

(Fig. 5e). This is because thermal stress produced around re-injection wells significantly perturbs the minimum effective principal stress field around the re-injection wells, causing stress concentration (more compressive) in the fault-parallel direction and stress relaxation (less compressive or more tensile) in the fault-normal direction (Fig. 5f). This stress perturbation modifies the permeability of fractured reservoir rocks by varying the aperture of underlying fractures. Rocks in the fault-normal direction are subjected to cooling contraction-induced permeability enhancement, which facilitates the flow of colder injected fluids.

The induced thermoelastic stress due to injection of cold fluids has a more pronounced effect on the stress state than the fluid pressure change and poroelastic stress. Since the onset of geothermal operations, the minimum effective principal stress change $\Delta\sigma'_3$ caused by thermoelastic stressing could exceed 4 MPa (the in-situ effective minimum principal stress at 1000 m depth), so regions immediately around re-injection wells are subjected to tensile stresses. After 10 years of geothermal operations, the minimum effective principal stress concentrated regions (coloured in red) extend over 2 km in the fault-parallel direction, whilst the relaxed regions (coloured in blue) over 1.2 km in the fault-normal direction (Fig. 5f). In addition, the contrast between the evolution of overpressurised regions and cooled regions implies that fluid flow migrates at a much faster pace than the heat transfer.

Fig. 6 presents fluid pressure, temperature, and minimum effective principal stress changes at measurement points over the modelled period in model scenarios with and without considering cooling contraction. Fluid pressure changes at different locations in the cooling contraction scenario are slightly higher than those in the non-cooling contraction scenario, signifying the role of cooling contraction-induced permeability enhancement. The fluid pressure change at measurement point A throughout the modelled period ranges mostly between 0.5 MPa and 1.0 MPa, comparable to the field injection pressures maintained at ~0.8 MPa. Smaller fluid pressure changes are observed at measurement points away from the injection area in both fault-parallel and fault-normal directions (Fig. 6a and b). Fluid pressure changes at measurement points D and E located closer to the Skarðsmýrarfjall area are close to 0 or even become negative when injection rates are low or production rates are high.

The comparison between the two model scenarios reveals that when cooling contraction is considered, temperature drops slower in the fault-parallel direction (the measurement point A), but faster in the fault-normal direction (the measurement point F). This demonstrates the role of cooling contraction-induced permeability change on heat transfer, i.e., reduction in the fault-parallel direction and enhancement in the fault-normal direction. In the cooling contraction model scenario, the temperature at measurement point A drops significantly by ~50 °C during the 2.5 years of cold fluid injection, followed by much gentler decrease by a further 45 °C in the following years (Fig. 6c). The measurement point F begins to experience a temperature drop after 2 years of injection, and has a total temperature drop of ~20 °C over the modelled period (Fig. 6d). Temperature remains unchanged at other measurement points spaced farther away, implying that the thermodynamic front is restricted within 500 m around the injection wells even after 10 years of operation.

In the cooling contraction model scenario, the measurement point A



Fig. 6. Evolution of fluid pressure, temperature, and minimum effective principal stress changes at measurement points (from Fig. 5a) over the modelled period for cooling contraction and non-cooling contraction scenarios: (a), (c), (e) in the fault-parallel direction, and (b), (d), (f) in the fault-normal direction.

located within the injection area experiences a sharp decrease of 4 MPa in the minimum effective principal stress shortly after the cold fluid injection began, marking a rapid transition from bulk compression to extension of rocks (Fig. 6e). The tensile region expands in the fault-normal direction by 300 m (the measurement point F) in less than 0.3 years, by 600 m (the measurement point G) in 3.3 years, and by 900 m in over 10 years (Fig. 6f). Minimum effective principal stresses in the fault-parallel direction are gradually concentrated, yielding an increase of ~12 MPa within 500 m away from the injection area (the measurement point B), but less than 5 MPa more than 1000 m away (measurement points C, D and E) after 10 years of injection (Fig. 6e). In contrast, minimum effective principal stress changes due to poroelastic response alone are negligible at different locations in the non-cooling contraction model scenario.

5.2. *Fracture slip susceptibility at Hellisheiði*

Fig. 7 presents modelled stress and permeability distribution on the fracture networks in the modelled region before fluid re-injection started. Large initial fracture shear stresses are produced in directions other than fault-parallel (NNE-SSW trending fractures, partly Set 1) and fault-normal (WNW-ESE trending fractures, partly Set 3) directions, and the maximum fracture shear stress could reach up to 35 MPa (Fig. 7a). In contrast, initial normal effective stresses are equal to the maximum

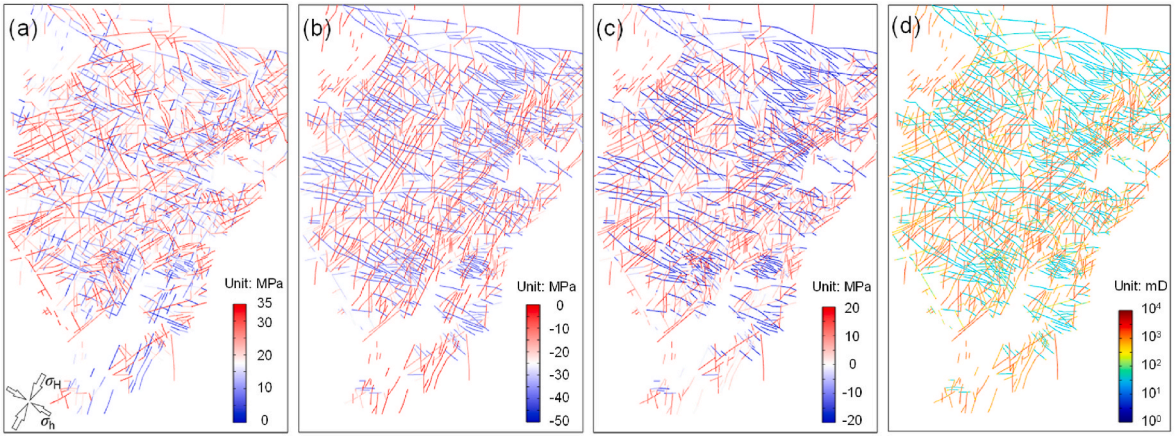


Fig. 7. Modelled stress and permeability distribution on the fracture networks at 1000 m depth in the modelled region before fluid re-injection started in September 2011: (a) shear stress along fractures τ, (b) normal effective normal stress on fractures $-f(\sigma - p)$ (positive for compression, thus the minus sign), (c) Coulomb failure stress along fractures CFS $= \tau - f(\sigma - p)$, and (d) effective fracture permeability k_{eff} (assuming a fracture zone width of 10 m).

horizontal effective principal stress on NNE-SSW trending fractures (partly Set 1), and equal to the minimum horizontal effective principal stress on WNW-ESE trending fractures (partly Set 3) (Fig. 7b). Considering combined effects of the two, Coulomb failure stresses are positive for NE-SW trending (partly Set 1) and N-S trending fractures (Set 2), and negative for WNW-ESE trending fractures (partly Set 3) (Fig. 7c). According to the Mohr-Coulombs failure criterion, the maximum Coulomb failure stress is achieved at 29.5° (45° - $\varphi/2$, φ being the friction angle which takes 31° for a friction coefficient of 0.6) from the NNE-SSW direction, i.e., roughly along the NE-SW and N-S directions, which are consistent with the observations. Fractures with positive Coulomb failure stresses are likely to have already slipped at their initial states. Therefore, the following analysis of fracture stress states will focus on the Coulomb failure stress change, rather than the absolute value of the Coulomb failure stress.

Fig. 8 presents modelled stress changes on the fracture networks over short (1 month), intermediate (1 year) and long-term (10 years) after geothermal operations started in the two model scenarios. In both scenarios, fluid pressure in the fractures increases around the Húsmúli area, and decreases around the Skarðsmýrarfjall area throughout the modelled period (Fig. 8a and d). The bulk expansion caused by fluid injection is opposed by increased compressive stress of a lesser amount (coloured in blue) around the Húsmúli area, and the opposite is true around the Skarðsmýrarfjall area (Fig. 8b). This fluid pressure change barely leads to shear stress changes along fracture planes (Fig. 8c).

When the cooling contraction is considered, the normal stress change is influenced by both poroelastic stressing and thermoelastic stressing (Fig. 8e). The thermal contraction due to injection of cold fluids results in lower compressive stresses (coloured in red) in surrounding fractures oriented perpendicular to the radial direction of the re-injection wells at the Húsmúli area (Fig. 8e). The thermal contraction also increases the shear stress along fracture planes (and the deviatoric stress in reservoir rocks) around the injection wells in the fault-normal direction, and decreases that in the fault-parallel direction (Fig. 8f). Whist the poroelastic stressing is dominant in the short-term after geothermal operations, the thermoelastic stressing prevails in terms of both the magnitude and areal extent in the intermediate- and long-term (Fig. 8e and f).

Fig. 9 presents modelled Coulomb failure stress changes on the fracture networks for both model scenarios at different times after geothermal operations started. In the non-cooling contraction scenario, fractures around the Húsmúli area are predominantly characterised by enhanced slip susceptibility (positive Coulomb failure stress changes ΔCFS), and those around the Skarðsmýrarfjall area by suppressed slip susceptibility (Fig. 9a). Both regions of enhanced and suppressed enhanced slip susceptibility represent preferential fluid flow pathways, which are oriented in alignment with the regional fault strike throughout the modelled period.

When the cooling contraction is considered, the fracture slip susceptibility is similar to that in the non-cooling contraction scenario in the first month of geothermal operations, implying the dominant control of fluid pressure and poroelastic stressing (Fig. 9d). After 1 year, thermoelastic stressing leads fracture slip susceptibility enhanced regions to

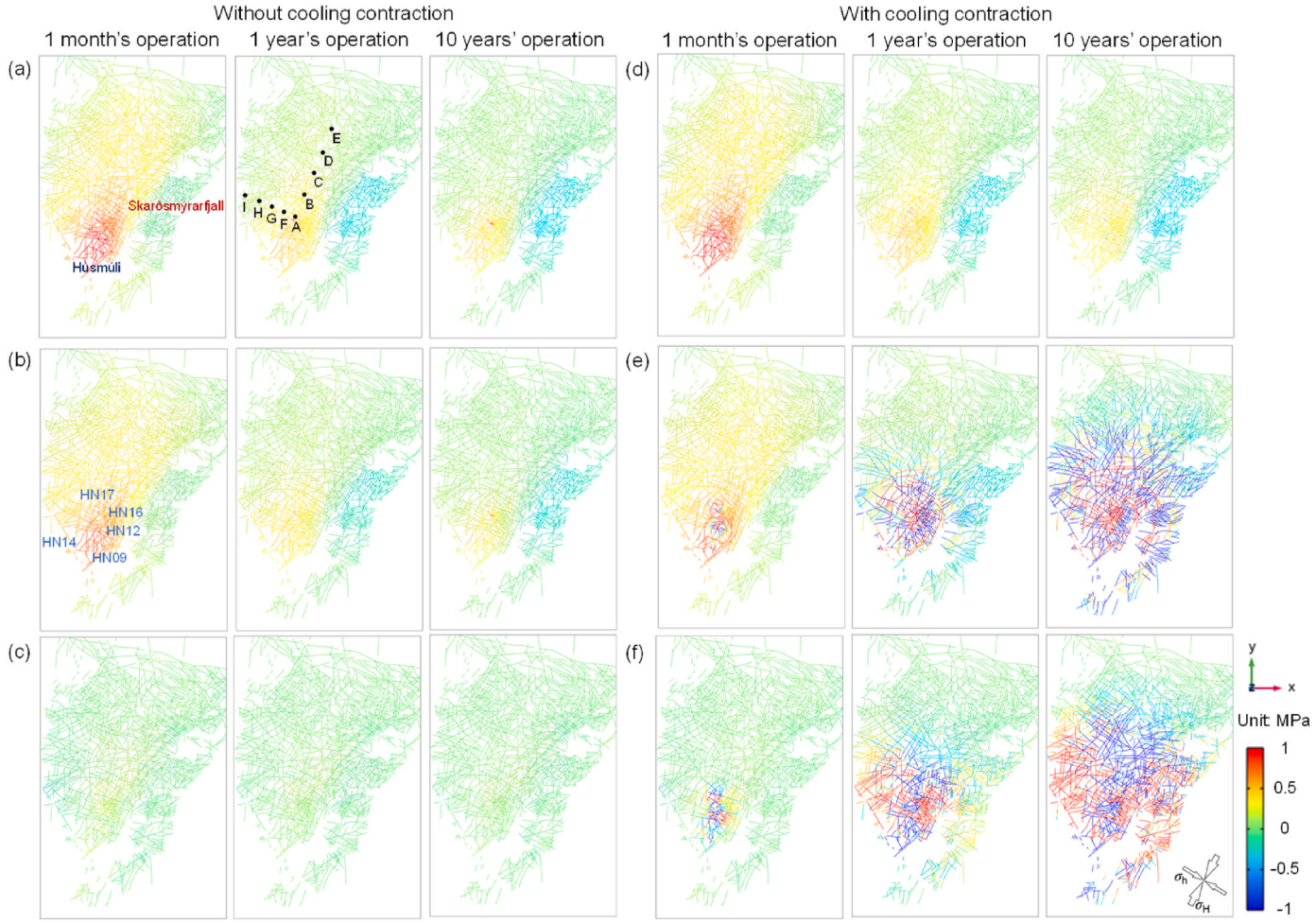


Fig. 8. Modelled stress changes on the fracture network at 1000 m depth over short (1 month), intermediate (1 year) and long-term (10 years) after geothermal operations started at Húsmúli and Skarðsmýrarfjall in non-cooling contraction and cooling contraction model scenarios: (a) and (d) fluid pressure change $f\Delta p$, (b) and (e) normal stress change $-f\Delta\sigma$ (positive for compression, thus a minus sign), (c) and (f) shear stress change $\Delta\tau$.

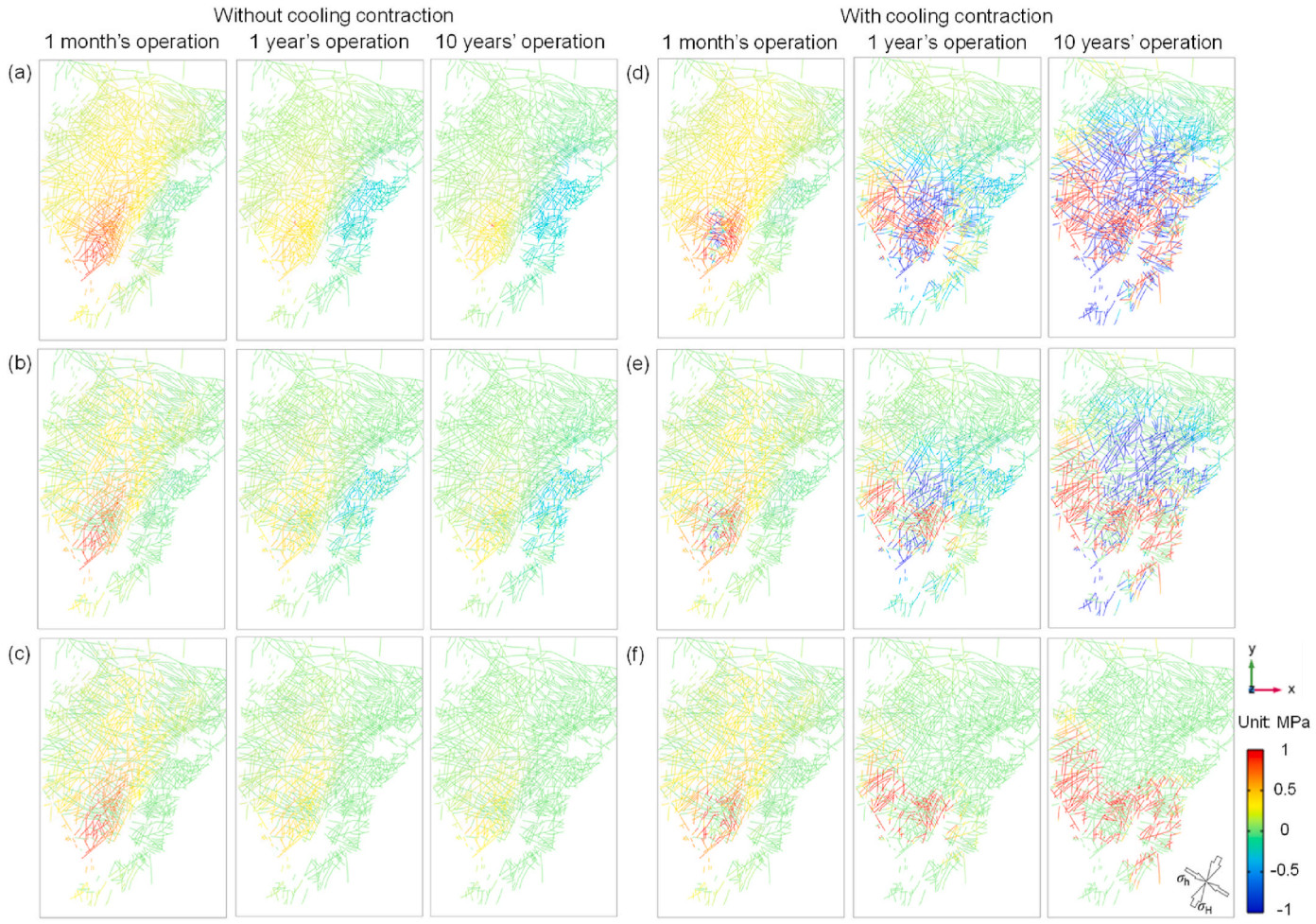


Fig. 9. Modelled Coulomb failure stress changes $\Delta CFS = \Delta\tau - f(\Delta\sigma - \Delta p)$ on the fracture network at 1000 m depth over short (1 month), intermediate (1 year) and long-term (10 years) after geothermal operations started at Húsmúli and Skarðsmýrarfjall in non-cooling contraction and cooling contraction model scenarios: (a) and (d) all fractures, (b) and (e) initially susceptible fractures (CFS >0), and (c) and (f) fractures that remained as susceptible to slip after re-injection started (CFS >0 and ΔCFS >0).

extend in the fault-normal direction, and suppressed regions in the fault-parallel direction (Fig. 9d). Regions with enhanced and inhibited fracture slip susceptibility continue to expand extensively around the re-injection wells during 10 years of operation, reaching more than 2000 m away from the wells in the fault-normal direction (Fig. 9d). Noticeably, Coulomb failure stress change in fractures around re-injection wells is considerably elevated in the cooling contraction model scenario, indicating the dominant role of thermal effect over hydrogeological effect in the intermediate- and long-term.

Considering the combined effects of in-situ stresses and geothermal operations on fracture slip susceptibility, fractures that were initially susceptible to slip (CFS >0) and those remained as being susceptible after re-injection started (CFS >0 and ΔCFS >0) are displayed in Fig. 9b and e and Fig. 9c and f, respectively. Fractures that initially started as susceptible to slip mostly belonged to the Fracture Sets 1 and 2 (Fig. 9b and e), while those that remained susceptible after re-injection started are a subset of the above with positive ΔCFS (Fig. 9c and f). In the non-cooling contraction scenario, fractures that remained as susceptible to slip fell on the preferential fluid flow path within the overpressurised region throughout the modelled period (Fig. 9c). On the other hand, in the case of cooling contraction, fractures that remained susceptible to slip gradually manifested a two-lobed pattern after 1 year of geothermal operations (Fig. 9f). Slippage of these fractures is considered as sources for seismicity at the Hellisheiði geothermal field.

To examine the long-term evolution of fracture slip susceptibility, Coulomb failure stress change ΔCFS for NNE-trending fractures at measurement points over the modelled period in both model scenarios are plotted in Fig. 10. When cooling contraction is not considered, ΔCFS is elevated to relatively low positive values immediately around re-injection wells (0.8 MPa for Point A), so as those along both fault-parallel direction (0.7 MPa for Points B and C) and fault-normal directions (0.65 MPa for Point F, and 0.45 MPa for point G) (Fig. 10a and b, dashed lines). These ΔCFS values maintain at low levels throughout the modelled period.

When cooling contraction is modelled, ΔCFS increases rapidly over time within 600 m distance from the injection area in the fault-normal direction (as at measurement points A and F), but much gently more than 900 m away (as at measurement points G, H and I) (Fig. 10b, solid lines). In contrast, ΔCFS continuously decreases away from the injection area in the fault-parallel direction, and the measurement point B has the minimum ΔCFS, which could be as low as −7 MPa after 10 years of cold fluids injection (Fig. 10a, solid lines). The evolution of Coulomb failure stress change ΔCFS in Fig. 10a and (b) has an opposite trend with that of the minimum effective principal stress changes $\Delta\sigma'_3$ in Fig. 6e and (f), implying that the latter (predominantly caused by thermoelastic stressing) dominates the slip tendency of fracture networks.

Fig. 11 presents the advance of hydrodynamic and thermal fronts at the Hellisheiði geothermal field at different times in the two model scenarios. A hydrodynamic front of 0.5 MPa pressure increase and a thermal front of 10 °C temperature decrease are used to illustrate the

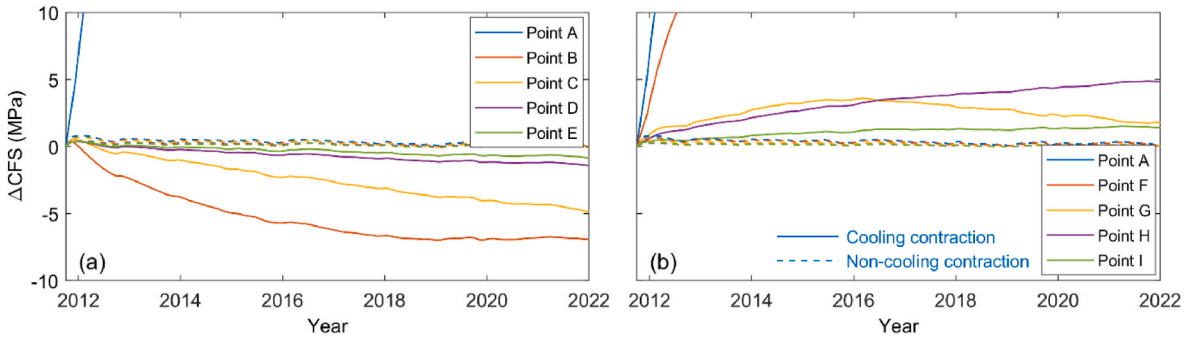


Fig. 10. Evolution of Coulomb failure stress change ΔCFS for NNE-trending fractures at measurement points (from Fig. 8a) over the modelled period at Húsmúli and Skarðsmýrarfjall for cooling contraction and non-cooling contraction scenarios: (a) in the fault-parallel direction, and (b) in the fault-normal direction.

evolution of fluid pressure and temperature fields, respectively. When the cooling contraction is not considered, the hydrodynamic fronts manifest oval-shaped patterns at different times, delineating the preferential fluid flow path around the injection area (Fig. 11a). The hydrodynamic front responds fast following the fluctuating field injection rates over time, reflecting the great hydraulic conductivity of the fracture network. For such permeable reservoir formations, fluid injection at a constant injection pressure would lead to quasi-steady-state flow conditions within 0.1 year after geothermal operations started.[48] In comparison, thermal fronts emerge in the immediate vicinity of re-injection wells, and gradually coalesce into a large one over the operational period (Fig. 11c). The area of cooled regions is less than that of overpressured regions, and the thermal front is much less smooth than that of the hydrodynamic front, both manifesting the limited areal influence of temperature.

When the cooling contraction is modelled, the hydrodynamic front advances to a relatively larger region over the geothermal period (Fig. 11b), as a consequence of the cooling contraction-induced permeability enhancement of the faulted reservoir. The broad fluid pressure distribution accelerates the convection driven by the Darcy's velocity field, which in turn intensifies the cooling contraction effect. As a result, time-lapse thermal fronts advance farther (Fig. 11d) in comparison to those in the non-cooling contraction model scenario (Fig. 11c).

6. Discussion

6.1. Model performance against field monitored seismicity

To examine the performance of the model developed, the distribution of fractures modelled as being susceptible to slip were compared against field monitored seismicity at the Húsmúli area at different times over the 10-year period between September 2011 and September 2021 (with a seismic monitoring gap between May 2012 and December 2016) (Fig. 12). Field monitored seismicity are superimposed on the slip susceptible fracture patterns. The model results and field observations achieved overall consistency across various time scales over the modelled period. At the onset of geothermal operations (September 2011), field monitored seismicity distributed along the preferential fluid flow path, which is delineated by the modelled slip susceptible fractures (Fig. 12a). Within 1 year of geothermal operations, whilst seismicity persisted along the local fault strike, some seismic events emerged to the west of the injection wells, i.e., predominantly within the left lobe of the two-lobe-shaped susceptibility enhanced region gradually formed (Fig. 12b and c). Since then, modelled slip susceptible fractures maintain this two-lobe distribution pattern, although the region populated with slip susceptible fractures gradually expands (Fig. 12d–h). The distribution of field monitored seismicity also expanded over time, and mostly overlapped with the fractures modelled as susceptible to slip (Fig. 12f–h). Seismicity tended to locate within the left lobe, suggesting less pronounced stress and pressure perturbations to the southeast of the injection wells. This observation is in agreement with observations from tracer tests carried out during 2013–2015, where the re-injection wells are not well communicated hydraulically with the southeast part.[49]

The distribution and evolution of Coulomb Failure Stress Changes from the current model were also compared with those from a 3D coupled THM model implemented without explicitly incorporating fracture networks by the authors[48] (Fig. 13). This previous model used comparable geomechanical, hydrological and thermodynamic parameters for reservoir rocks, and only simulated reservoir response to cold fluids injection at Húsmúli in a 5 km × 6 km model domain. The only difference in evaluating the Coulomb failure stress change ΔCFS lies in orientations considered for fractures to slip: the fixed NNW-SSW fault strike in the fracture-free model, but the respective fracture orientation of each fracture plane considered in the current model. From Fig. 9d, e and f and Fig. 13, the spatial extent of seismic susceptibility enhanced and suppressed regions in general compares favourably between the two models across different time scales after geothermal operations started. Compared to the fracture-free model, the slip susceptibility for fractures in the current model is more inhibited around the Skarðsmýrarfjall area due to geothermal production.

It is worth mentioning that uncertainties exist for a range of parameters used in the coupled THM model, including stress and geological parameters (the maximum and minimum horizontal principal stresses, stress orientation, fluid pressure, fault dip, etc.)[10,26,50,51] and material parameters (porosity, permeability, Young's modulus, Poisson's ratio, friction coefficient, Biot's coefficient, thermal expansion coefficient, heat capacity, thermal conductivity, etc.).[52,53] Parametric investigations of material parameters have shown that the thermal expansion coefficient and permeability are amongst the most sensitive factors to the geomechanical stability in geothermal systems.[52] The potential for fault re-activation is also considered to be highly sensitive to the stress field and fault friction.[51] In particular, a friction coefficient of 0.6 was assumed to calculate the Coulomb failure stress change in this work, representing the low end of the range of 0.6–0.85 reported by Byerlee.[54] This is in line with previous research which assumed the same friction coefficient for hydraulically conductive faults (e.g.,[21,22,55]). The relatively low friction coefficient provides a conservative assessment of fault stability. When the friction coefficient is within the range of 0.6–0.85, there would be less fractures that were initially susceptible to slip (CFS >0), and less fractures that would remain as being susceptible after re-injection started (CFS >0 and ΔCFS >0). This would cause a more limited spatial extent of modelled slip susceptible fractures as compared to field monitored seismicity in Fig. 12. Uncertainties in other stress, geological and material parameters were largely constrained by comprehensive previous studies (Table 1), and the existing uncertainties do not change main conclusions obtained from the modelling work. Nevertheless, it would be beneficial to carry out further parametric investigations to refine model results and provide probabilistic evaluations of the potential for fault re-activation.

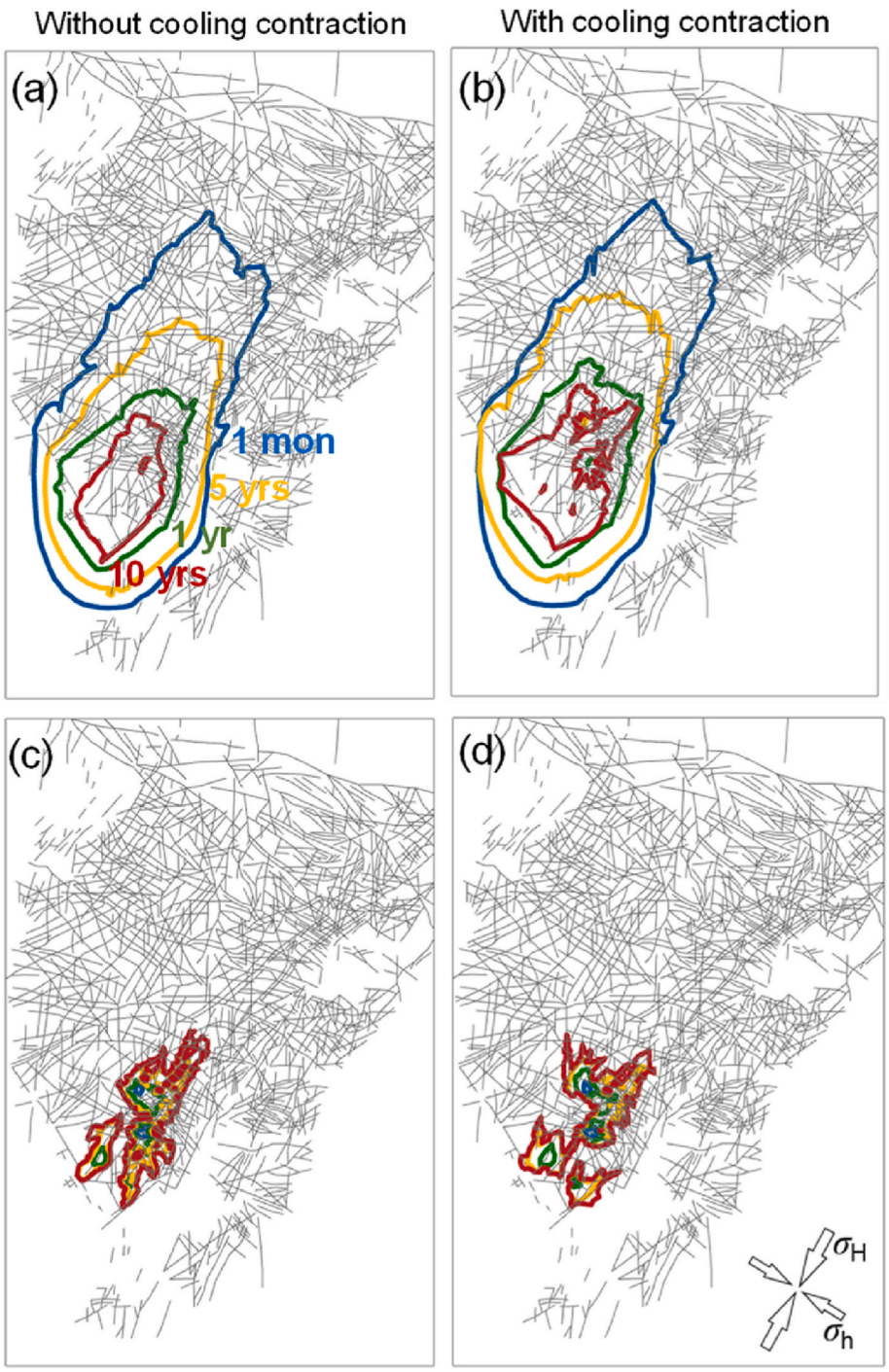


Fig. 11. Modelled time-lapse hydrodynamic and thermal fronts at the Hellisheiði geothermal field at different times at Húsmúli and Skarðsmýrarfjall for cooling contraction and non-cooling contraction scenarios: (a), (c) hydrodynamic front of 0.5 MPa, and (b), (d) thermal front of −10 °C.

6.2. Role of fracture systems on the coupled THM behaviour

A distinctive feature of the coupled THM model developed is the inclusion of field mapped, interconnected conductive fracture systems to explicitly model fluid flow channels in reservoir rocks, as opposed to a bulk of faulted regions populated with uniform properties.[27,48] This allows the evaluation of slip susceptibility of individual fractures by means of Coulomb failure stress change or any other slip susceptibility indicators, such as the slip tendency. In addition, the fracture slip susceptibility under the cooling contraction effect, which was rarely evaluated and compared against field observations, has also been investigated.

This model demonstrates the significant role of fracture networks on the fluid flow and heat transfer behaviour and the evolution of fracture slip susceptibility associated with geothermal operations. In the fluid flow and heat transfer process, the expansion of overpressurised and cooled regions is controlled by preferential fluid flow pathways, which are in turn dictated by the distribution, connectivity and intensity of natural fractures with highly anisotropic permeabilities.[56–58] In the stress and deformation response of reservoirs, fracture apertures vary due to poroelastic and thermoelastic stressing and further modify fracture permeabilities. Also, the fracture orientation has significant impacts

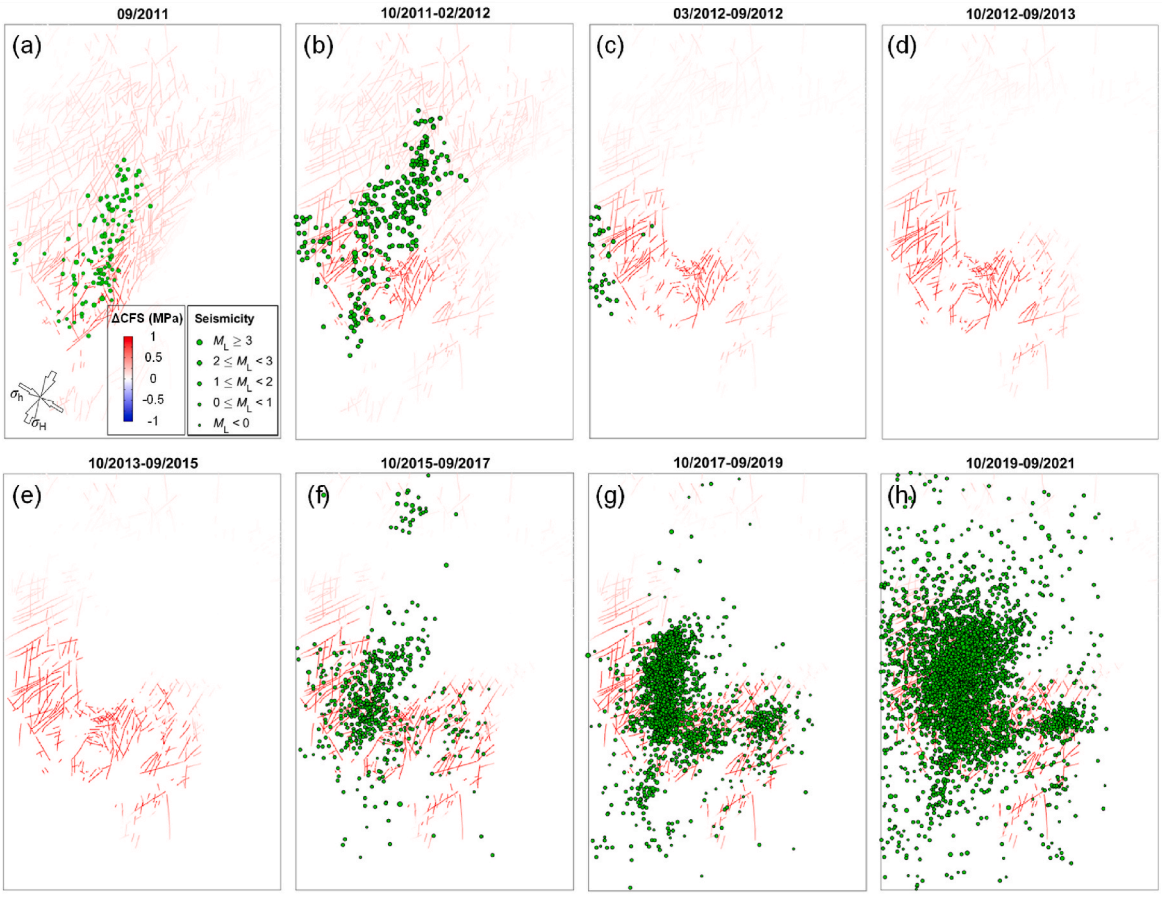


Fig. 12. Comparison between modelled slip susceptible fractures in the cooling contraction scenario and field monitored seismicity at Húsmúli at different times over a 10-year period between 2011 and 2021 (with a seismic monitoring gap between May 2012 and December 2016): (a) 1 month, (b) 0.5 year, (c) 1 year, (d) 2 years, (e) 4 years, (f) 6 years, (g) 8 years, and (h) 10 years after geothermal operations started.

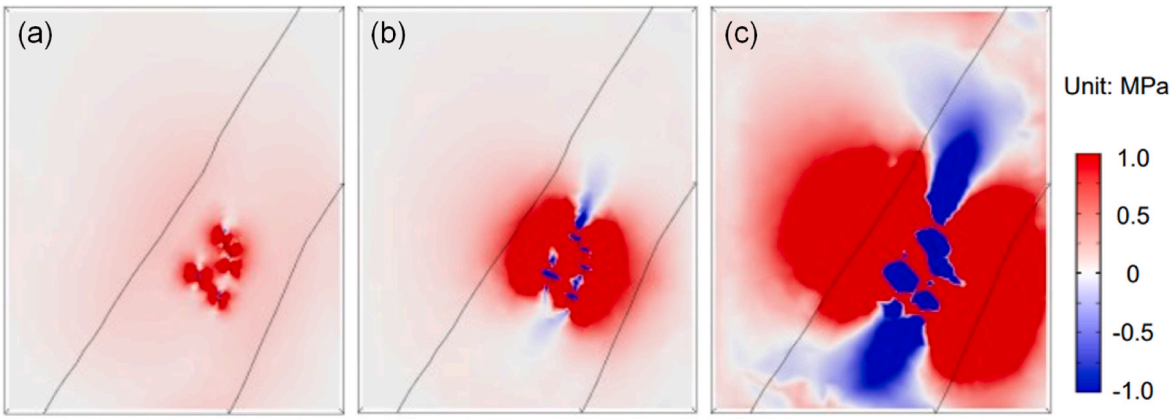


Fig. 13. Modelled Coulomb failure stress change ΔCFS at 1000 m depth at the Húsmúli area of Hellisheiði geothermal field in a fracture-free, 3D coupled THM model: (a) 0.1 year, (b) 1 year, and (c) 10 years after fluid re-injection started (after[48]).

on slip susceptibility for different fracture sets even under the same stress conditions (Fig. 7).

It is worth mentioning that several simplifications were made in modelling the hydromechanical behaviour of fracture systems in the current model. First, the current model, which is implementing an elastic constitutive model, did not consider elastoplastic behaviour such as rock damage and failure, therefore, tensile failure zones around re-injection wells and shear failure zones near fracture tips were not realistically modelled. Second, explicit fracture slippage and propagation, as well as consequent stress re-distribution and shear dilution-induced fracture aperture change, were not modelled due to high computational costs, which may cause deviations in the stress field around fractures that have already slipped before geothermal operations started. Third, fracture permeabilities assigned based on a uniform initial fracture aperture may not accurately represent the wide spread of permeability distribution for fractures in the same fracture set. Fracture permeability usually has a positive correlation with fracture length, and the permeability for different fractures in the same fracture set may span

across several orders of magnitude.[59,60] One common approach to further consider this variability of fracture permeability is to adopt the fracture aperture-to-length scaling relationship, which takes linear[61] or square-root[62] forms based on various assumptions. An alternative approach is to parameterise the distribution of fracture permeabilities based on approximate scaling functions derived from laboratory and field measured fracture permeabilities.[63,64] Nevertheless, the focus of this work is placed on capturing the hydrological behaviour at the fracture network scale, rather than the variability of fracture permeability distribution, therefore, this model is considered to effectively represent the field reservoir response and fracture slip susceptibility under combined actions of hydraulic and thermal effects.

6.3. Competing role of cooling contraction and fluid overpressure on fracture slip susceptibility

In this work, the non-cooling contraction model scenario represents the effect of poroelastic effect alone on fracture slip susceptibility, whilst the cooling contraction model scenario demonstrates the role of thermoporoelastic effect. Based on thermoporoelastic theory,[65] both cooling contraction of reservoir rocks and fluid overpressure associated with fluids injection can lead to conditions towards increased potential for induced seismicity. Under unconstrained stress states, the contribution of thermoelastic and poroelastic stresses around fluid injection wells can be quantified by the ratio of temperature change to fluid pressure change $\Delta T/\Delta p$, as well as rock hydrological and thermodynamic properties.[66] The $\Delta T/\Delta p$ value around injection wells at geothermal fields is influenced by both fluid flow and heat transfer in surrounding regions, which may lead to competing effects between cooling contraction and fluid overpressure on fracture slip susceptibility in the long term.

For the Hellisheiði reservoir formations embedded with a highly conductive fracture system, quasi-static fluid flow conditions can be reached within one month after the start of re-injection.[48] Even with fluctuating injection rates under field operational conditions, the fluid pressure change is kept well below 1 MPa across the majority of the reservoir region (Fig. 6a and b). Taking the wellhead pressure of 8 bar as an approximation of the fluid pressure change Δp, the ratio $\Delta T/\Delta p$ is only influenced by the temperature change ΔT. The areal extent of cooled regions grows monotonically, preferentially in the fault-normal direction under the influence of cooling contraction-induced permeability change (Fig. 11d). In addition, the temperature in cooled regions continues to drop, although the cooling rate gradually becomes slower as cooled regions expand to increasingly larger volumes (Fig. 6d). Therefore, it is believed that fractures currently susceptible to slip will continue to be characterised by high slip potential, and that regions with enhanced fracture slip susceptibility will continue to expand in the long term, given the existence of regional natural fracture systems.

7. Conclusions

This paper presents the development and application of a coupled THM model containing fracture networks to simulate geothermal fluids extraction and re-injection process over a 10-year period at the Hellisheiði geothermal field. Model results have shown that fracture networks representing preferential fluid flow pathways have a pronounced effect on the fluid pressure, stress and temperature distribution. Due to the nature of fluid flow and heat transfer in fractured rocks, the hydrodynamic front outpaces the thermal front, and fluid overpressured regions are larger than cooled regions. The $\Delta T/\Delta p$ value around re-injection wells gradually increases over the geothermal operation period, which represents the dominant control of cooling contraction over fluid overpressure on the stress state in the long term.

The inclusion of fracture networks allows for the slip susceptibility evaluation on each individual fracture, which is more accurate than the previous fracture-free coupled THM modelling approach. Model results have shown that NE-SW and N-S trending fractures (Sets 1 and 2) are susceptible to slippage, or even have already slipped under in-situ stress conditions. At the onset of geothermal fluid re-injection, the slip susceptibility of fractures is enhanced around the Húsmúli area but suppressed around the Skarðsmýrarfjall area, as dominated by the fluid pressure and poroelastic stressing. Over the intermediate- and long-term, a two-lobed pattern is formed for fractures with enhanced slip susceptibility in the fault-normal direction around the Húsmúli area, driven by the thermoelastic stressing that gradually prevails over fluid pressure and poroelastic stressing. The distribution of modelled slip susceptible fractures compared favourably with that of recorded induced seismicity over the modelled period at the Hellisheiði geothermal field. Furthermore, model results suggested that regions with enhanced fracture slip susceptibility would continue to expand in the long term.

CRediT authorship contribution statement

Wenzhuo Cao: Writing – original draft, Methodology, Investigation, Formal analysis, Conceptualization. **Sevket Durucan:** Writing – review & editing, Supervision, Methodology, Funding acquisition. **Ji-Quan Shi:** Writing – review & editing, Methodology. **Anna Korre:** Writing – review & editing, Funding acquisition. **Thomas Ratouis:** Writing – review & editing, Validation, Data curation. **Vala Hjörleifsdóttir:** Writing – review & editing, Validation.

Declaration of competing interest

The authors declare that they have no known competing financial interests or personal relationships that could have appeared to influence the work reported in this paper.

Acknowledgements

This research was carried out as part of the project “Synergetic Utilisation of CO_2 storage Coupled with geothermal Energy Deployment - SUCCEED” funded through the ACT programme (Accelerating CCS Technologies, Horizon 2020 Project No 299670). Financial contributions made by the Department for Business, Energy & Industrial Strategy UK, the Ministry of Economic Affairs and Climate Policy, the Netherlands, the Scientific and Technological Research Council of Turkey and research partners Orkuveita Reykjavíkur/Reykjavik Energy Iceland (OR) and Istituto Nazionale di Oceanografia e di Geofisica Sperimentale Italy (OGS) are gratefully acknowledged. The authors also wish to thank the Swiss Seismological Service (SED) at ETH Zurich for their permission to use the Hengill (Iceland) seismic monitoring data from the COSEISMIQ network (http://networks.seismo.ethz.ch/en/networks/2c/).

Data availability

The authors do not have permission to share data.

References

1. Jiang C, Wang X, Zhang F, Deng K, Lei Q. Fracture activation and induced seismicity during long-term heat production in fractured geothermal reservoirs. *Rock Mech Rock Eng.* 2022;55(8):5235–5258.
2. Chen X, Nakata N, Pennington C, et al. The Pawnee earthquake as a result of the interplay among injection, faults and foreshocks. *Sci Rep.* 2017;7(1):4945. https://doi.org/10.1038/s41598-017-04992-z.
3. Hincks T, Aspinall W, Cooke R, Gernon T. Oklahoma's induced seismicity strongly linked to wastewater injection depth. *Science.* 2018;359(6381):1251–1255.
4. Dempsey D, Suckale J. Physics-based forecasting of induced seismicity at Groningen gas field, The Netherlands. *Geophys Res Lett.* 2017;44(15):7773–7782.
5. Snee JEL, Zoback MD. State of stress in the Permian Basin, Texas and New Mexico: implications for induced seismicity. *Lead Edge.* 2018;37(2):127–134.
6. Hennings PH, Snee JL, Osmond JL, et al. Injection-induced seismicity and fault-slip potential in the Fort Worth Basin, Texas. *Bull Seismol Soc Am.* 2019;109(5):1615–1634.

7. Fielding EJ, Sangha SS, Bekaert DPS, Samsonov SV, Chang JC. Surface deformation of north-central Oklahoma related to the 2016 Mw 5.8 Pawnee earthquake from SAR interferometry time series. *Seismol Res Lett*. 2017;88(4):971–982.
8. Schoenball M, Ellsworth WL. Waveform-relocated earthquake catalog for Oklahoma and Southern Kansas illuminates the regional fault network. *Seismol Res Lett*. 2017; 88(5):1252–1258. https://doi.org/10.1785/0220170083.
9. Feng C, Gao G, Zhang S, et al. Fault slip potential induced by fluid injection in the Matouying enhanced geothermal system (EGS) field, Tangshan seismic region, North China. *Nat Hazards Earth Syst Sci*. 2022;22(7):2257–2287.
10. Walsh FR, Zoback MD. Probabilistic assessment of potential fault slip related to injection-induced earthquakes: application to north-central Oklahoma, USA. *Geology*. 2016;44(12):991–994.
11. Salimzadeh S, Paluszny A, Nick HM, Zimmerman RW. A three-dimensional coupled thermo-hydro-mechanical model for deformable fractured geothermal systems. *Geothermics*. 2018;71(October 2017):212–224.
12. Chen Y, Zhao Z, Peng H. Convective heat transfer of water flow in intersected rock fractures for enhanced geothermal extraction. *J Rock Mech Geotech Eng*. 2022;14(1): 108–122.
13. Shi Y, Song X, Li J, Wang G, YuLong F, Geng L. Analysis for effects of complex fracture network geometries on heat extraction efficiency of a multilateral-well enhanced geothermal system. *Appl Therm Eng*. 2019;159, 113828.
14. Sun Z, Jiang C, Wang X, Zhou W, Lei Q. Combined effects of thermal perturbation and in-situ stress on heat transfer in fractured geothermal reservoirs. *Rock Mech Rock Eng*. 2021;54:2165–2181.
15. Li S, Feng XT, Zhang D, Tang H. Coupled thermo-hydro-mechanical analysis of stimulation and production for fractured geothermal reservoirs. *Appl Energy*. 2019; 247:40–59.
16. Gan Q, Elsworth D. Production optimization in fractured geothermal reservoirs by coupled discrete fracture network modeling. *Geothermics*. 2016;62:131–142.
17. Wang Y, Li T, Chen Y, Ma G. A three-dimensional thermo-hydro-mechanical coupled model for enhanced geothermal systems (EGS) embedded with discrete fracture networks. *Comput Methods Appl Mech Eng*. 2019;356:465–489.
18. Li X, Gao K, Feng Y, Zhang C. 3D geomechanical modeling of the Xianshuihe fault zone, SE Tibetan Plateau: implications for seismic hazard assessment. *Tectonophysics*. 2022;839, 229546.
19. Hemami B, Masouleh SF, Ghassemi A. 3D geomechanical modeling of the response of the Wilzetta Fault to saltwater disposal. *Earth and Planetary Physics*. 2021;5(6): 559–580.
20. Sun Z, Salazar-Tio R, Wu L, Bostrøm B, Fager A, Crouse B. Geomechanical assessment of a large-scale CO2 storage and insights from uncertainty analysis. *Geoenergy Science and Engineering*. 2023;224, 211596.
21. Cao W, Verdon JP, Tao M. Coupled poroelastic modeling of hydraulic fracturing-induced seismicity: implications for understanding the post shut-in ML 2.9 earthquake at the Preston New Road, UK. *J Geophys Res Solid Earth*. 2022;127(3), e2021JB023376. https://doi.org/10.1029/2021JB023376.
22. Fan Z, Eichhubl P, Gale JFW. Geomechanical analysis of fluid injection and seismic fault slip for the Mw 4.8 Timpson, Texas, earthquake sequence. *J Geophys Res Solid Earth*. 2016;121(4):2798–2812.
23. Morris A, Ferrill DA, Henderson DB. Slip-tendency analysis and fault reactivation. *Geology*. 1996;24(3):275–278.
24. Moeck I, Kwiatek G, Zimmermann G. Slip tendency analysis, fault reactivation potential and induced seismicity in a deep geothermal reservoir. *J Struct Geol*. 2009; 31(10):1174–1182.
25. Hennings PH, Nicot J, Gao RS, et al. Pore pressure threshold and fault slip potential for induced earthquakes in the Dallas-Fort worth area of North Central Texas. *Geophys Res Lett*. 2021;48(15), e2021GL093564.
26. Cao W, Durucan S, Cai W, et al. Probabilistic evaluation of susceptibility to fluid injection-induced seismicity based on statistics of fracture criticality. *Rock Mech Rock Eng*. 2022:1–23. Published online.
27. Cao W, Durucan S, Shi JQ, Cai W, Korre A, Ratouisc T. Induced seismicity associated with geothermal fluids re-injection: poroelastic stressing, thermoelastic stressing, or transient cooling-induced permeability enhancement? *Geothermics*. 2022;102, 102404.
28. Jin L, Curry WJ, Lippoldt RC, Hussenoeder SA, Bhargava P. 3D coupled hydro-mechanical modeling of multi-decadal multi-zone saltwater disposal in layered and faulted poroelastic rocks and implications for seismicity: an example from the Midland Basin. *Tectonophysics*. 2023;863, 229996. https://doi.org/10.1016/j.tecto.2023.229996.
29. Mahzari P, Stanton-Yonge A, Sanchez-Roa C, et al. Characterizing fluid flow paths in the Hellisheidi geothermal field using detailed fault mapping and stress-dependent permeability. *Geothermics*. 2021;94, 102127.
30. Ratouis TMP, Só Snæbjörnsdóttir, Voigt MJ, et al. Carbfix 2: a transport model of long-term CO2 and H2S injection into basaltic rocks at Hellisheidi, SW-Iceland. *Int J Greenh Gas Control*. 2022;114, 103586.
31. Batir JF. *Stress Field Characterization of the Hellisheidi Geothermal Field and Possibilities to Improve Injection Capabilities*. University of Iceland (Master's thesis); 2011.
32. Khodayar M. Fracture analysis from aerial imageries and correlation with triggered earthquakes by injection at Húsmúli, Hengill, South Iceland. Report Iceland GeoSurvey. *Iceland GeoSurvey, Report íSOR-2013/008*. 2013;23.
33. Khodayar M, Axelsson G, Steingrímsson B. Potential structural flow paths for tracers and source faults of earthquakes at Húsmúli, Hengill, South Iceland. In: *Technical Report 2015/035*. ÍSOR; 2015.
34. Juncu D, Árnadóttir T, Geirsson H, et al. Injection-induced surface deformation and seismicity at the Hellisheidi geothermal field, Iceland. *J Volcanol Geoth Res*. 2020; 391, 106337.
35. Li S, Zhang D. Three-dimensional thermoporoelastic modeling of hydrofracturing and fluid circulation in hot dry rock. *J Geophys Res Solid Earth*. 2023;128(2), e2022JB025673.
36. Rathnaweera TD, Wu W, Ji Y, Gamage RP. Understanding injection-induced seismicity in enhanced geothermal systems: from the coupled thermo-hydro-mechanical-chemical process to anthropogenic earthquake prediction. *Earth Sci Rev*. 2020, 103182. Published online.
37. Bandis SC, Lumsden AC, Barton NR. Fundamentals of rock joint deformation. *Int J Rock Mech Min Sci Geomech Abstracts*. 1983;20(6):249–268.
38. Palmer I, Mansoori J. How permeability depends on stress and pore pressure in coalbeds: a new model. *SPE Reservoir Eval Eng*. 1996;1(6):539–544. https://doi.org/10.2118/52607-PA.
39. Shi JQ, Durucan S. A model for changes in coalbed permeability during primary and enhanced methane recovery. *SPE Reservoir Eval Eng*. 2005;8(4):291–299.
40. Rutqvist J, Tsang CF. A study of caprock hydromechanical changes associated with CO2-injection into a brine formation. *Environ Geol*. 2002;42(2):296–305.
41. Lei Q, Doonechaly NG, Tsang CF. Modelling fluid injection-induced fracture activation, damage growth, seismicity occurrence and connectivity change in naturally fractured rocks. *Int J Rock Mech Min Sci*. 2021;138, 104598.
42. Zhu WC, Wei CH. Numerical simulation on mining-induced water inrushes related to geologic structures using a damage-based hydromechanical model. *Environ Earth Sci*. 2011;62(1):43–54. https://doi.org/10.1007/s12665-010-0494-6.
43. Schneider E, Burrus J, Wolf S. Modelling overpressures by effective-stress/porosity relationships in low-permeability rocks: empirical artifice or. In: *Basin Modelling: Advances and Applications: Proceedings of the Norwegian Petroleum Society Conference, 13-15 March 1991, Stavanger, Norway*. 3. Elsevier Science Limited; 1993:333.
44. Heinze T, Hamidi S. Heat transfer and parameterization in local thermal non-equilibrium for dual porosity continua. *Appl Therm Eng*. 2017;114:645–652.
45. Stefánsson V, Sigurðsson Ó, Guðmundsson Á, Franzson H, Gó Friðleifsson, Tulinius H. Core measurements and geothermal modelling. In: *Second Nordic Symposium on Petrophysics*. 1997:199–220.
46. Snæbjörnsdóttir SÓ, Wiese F, Fridriksson T, Ármansson H, Einarsson GM, Gislason SR. CO2 storage potential of basaltic rocks in Iceland and the oceanic ridges. *Energy Proc*. 2014;63:4585–4600.
47. Juncu D, Árnadóttir T, Hooper A, Gunnarsson G. Anthropogenic and natural ground deformation in the Hengill geothermal area, Iceland. *J Geophys Res Solid Earth*. 2017; 122(1):692–709.
48. Cao W, Durucan S, Ratouis T, Shi JQ, Korre A, Hjörleifsdóttir V. Role of cooling contraction and fluid overpressure on induced seismicity: an investigation into field behavior at the Carbfix2 CO2 reinjection site, Hellisheiði geothermal power plant, Iceland. In: *Proceedings of the 16th Greenhouse Gas Control Technologies Conference (GHGT-16)*. 2022.
49. Kristjánsson BR, Axelsson G, Gunnarsson G, Gunnarsson I, Óskarsson F. Comprehensive tracer testing in the hellisheidi geothermal field in SW-Iceland. In: *Proceedings, 41st Workshop on Geothermal Reservoir Engineering*. 730. 2016.
50. Shen LW, Schmitt DR, Schultz R. Frictional stabilities on induced earthquake fault planes at Fox Creek, Alberta: a pore fluid pressure dilemma. *Geophys Res Lett*. 2019; 46(15):8753–8762.
51. Seithel R, Gaucher E, Mueller B, Steiner U, Kohl T. Probability of fault reactivation in the bavarian molasse basin. *Geothermics*. 2019;82:81–90.
52. Zhang L, Dieudonné AC, Daniilidis A, et al. Thermo-hydro-mechanical modeling of geothermal energy systems in deep mines: uncertainty quantification and design optimization. *Appl Energy*. 2024;377, 124531.
53. Zhang S, Ma X. Global frictional equilibrium via stochastic, local Coulomb frictional slips. *J Geophys Res Solid Earth*. 2021;126(7), e2020JB021404.
54. Byerlee J. Friction of rocks. In: *Rock Friction and Earthquake Prediction*. Springer; 1978:615–626.
55. Ito T, Zoback MD. Fracture permeability and in situ stress to 7 km depth in the KTB scientific drillhole. *Geophys Res Lett*. 2000;27(7):1045–1048.
56. Ghassemi A, Zhou X. A three-dimensional thermo-poroelastic model for fracture response to injection/extraction in enhanced geothermal systems. *Geothermics*. 2011;40(1):39–49.
57. Koh J, Roshan H, Rahman SS. A numerical study on the long term thermo-poroelastic effects of cold water injection into naturally fractured geothermal reservoirs. *Comput Geotech*. 2011;38(5):669–682.
58. Kang F, Li Y, Huang X, Li T. Competition between cooling contraction and fluid overpressure on aperture evolution in a geothermal system. *Renew Energy*. 2022. Published online.
59. Odling NE, Harris SD, Knipe RJ. Permeability scaling properties of fault damage zones in siliclastic rocks. *J Struct Geol*. 2004;26(9):1727–1747.
60. Bisdom K, Bertotti G, Bezerra FH. Inter-well scale natural fracture geometry and permeability variations in low-deformation carbonate rocks. *J Struct Geol*. 2017;97: 23–36. https://doi.org/10.1016/j.jsg.2017.02.011.
61. Renshaw CE, Park JC. Effect of mechanical interactions on the scaling of fracture length and aperture. *Nature*. 1997;386(6624):482–484. https://doi.org/10.1038/386482a0.
62. Olson JE. Sublinear scaling of fracture aperture versus length: an exception or the rule? *J Geophys Res*. 2003;108(B9):2413. https://doi.org/10.1029/2001JB000419.
63. Frash LP, Welch N, Carey JW. Progress towards a scaling relationship between shear fracture length, aperture, and permeability. In: *ARMA US Rock Mechanics/Geomechanics Symposium. ARMA*. 2020. ARMA-2020.

64. Baghbanan A, Jing L. Hydraulic properties of fractured rock masses with correlated fracture length and aperture. *Int J Rock Mech Min Sci*. 2007;44(5):704–719.
65. Wang HF. *Theory of Linear Poroelasticity with Applications to Geomechanics and Hydrogeology*. Princeton University Press; 2017.
66. Segall P, Fitzgerald SD. A note on induced stress changes in hydrocarbon and geothermal reservoirs. *Tectonophysics*. 1998;289(1-3):117–128.